JACS
JOURNAL OF THE AMERICAN CHEMICAL SOCIETY
Article
Cite This: J. Am. Chem. Soc. 2018, 140, 13775−13785
pubs.acs.org/JACS

Electrocatalytic Study of the Oxygen Reduction Reaction at Gold Nanoparticles in the Absence and Presence of Interactions with SnO_x Supports

Nevena Ostojic,[†] Zhiyao Duan,[†] Aigerim Galyamova, Graeme Henkelman,* and Richard M. Crooks*

Department of Chemistry, Center for Electrochemistry, and Texas Materials Institute, The University of Texas at Austin, 105 East 24th Street, Stop A5300, Austin, Texas 78712-1224, United States

Supporting Information

ABSTRACT: Here we report that density functional theory (DFT) can be used to accurately predict how Au nanoparticle (NP) catalysts cooperate with SnO_x (x = 1.9 or 2.0) supports to carry out the oxygen reduction reaction (ORR). Specifically, dendrimers were used to encapsulate AuNPs and prevent their interactions with the underlying SnO_x supports. After removal of the dendrimers, however, the AuNPs are brought into direct contact with the support and hence feel its effect. The results show that both $SnO_{1.9}$ and $SnO_{2.0}$ supports strongly enhance the electrocatalytic properties of AuNPs for the ORR. In the case of AuNP interaction with a $SnO_{1.9}$ support, the number of electrons involved in the ORR (n_{eff}) increases from 2.1 ± 0.2 to 2.9 ± 0.1 following removal of the dendrimers, indicating an increased preference for the desired four-electron product (water), while the overpotential decreases by 0.32 V. Similarly, direct interactions between AuNPs and a $SnO_{2.0}$ support result in an increase in n_{eff} from 2.2 ± 0.1 to 3.1 ± 0.1 and a reduction of the overpotential by 0.28 V. These experimental results are in excellent agreement with the theoretically predicted onset potential shift of 0.30 V. According to the DFT calculations, the observed activity enhancements are attributed to the existence of anionic Au resulting from electron transfer from surface oxygen vacancies within the SnO_x supports to the AuNPs. This theoretical finding was confirmed experimentally using X-ray photoelectron spectroscopy. Importantly, the calculations reported here were performed prior to the experiments. In other words, this study represents an unusual case of theory accurately predicting the electrocatalytic manifestation of strong metal support interactions.

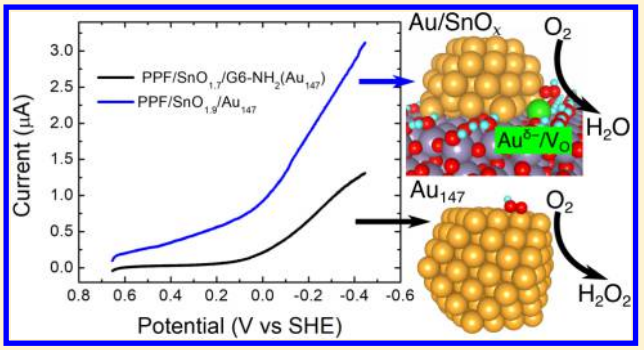

INTRODUCTION

Strong metal−support interactions (SMSIs) are well-known to influence the catalytic properties of supported catalysts.[1−4] Since the term SMSI was first introduced in 1978,[5,6] extensive theoretical[7−12] and experimental[13−19] efforts have been directed toward understanding and more efficiently utilizing such interactions. Most experimental studies relating to SMSI have involved gas-phase heterogeneous catalysis, while only a few have been carried out using electrochemical systems like that described here. This is because most active supports are insulators (oxides and nitrides), and one does not usually think of using insulating electrodes for electrocatalysis. Nevertheless, there have been a few very clever electrochemical studies in which support effects have been shown to be important.[20−24]

The Adzic group reported one of the first model electrocatalyst systems designed to better elucidate the role of the metal/metal-oxide interface.[15,16,20,21] For example, they constructed an inverse catalyst by depositing SnO_2 nanoparticles (NPs) onto a Pt electrode and showed that it was more effective for the methanol oxidation reaction (MOR) than Pt alone.[25] More specifically, they showed that the degree of effectiveness of the inverse electrocatalyst exhibited a strong dependence on the size of the SnO_2 NPs and hence the area of the Pt-SnO_2 interface. Theory suggested that the Pt−Sn electronic interactions, and the structural flexibility of smaller SnO_2 NPs, result in a weaker adsorption of OH species leading to more efficient oxidation of CO, a MOR intermediate that poisons Pt.

In addition to inverse catalysts, a few other systems have been used to study SMSIs for electrocatalytic reations.[13,14,18] For example, recently the Roziere group examined the beneficial effects of SnO_2 and doped-SnO_2 substrates on PtNP activity for the ORR.[22] In their experiments, Nb and Sb-doped SnO_2 tubes were prepared by electrospinning and subsequently modified with ∼4 nm PtNPs. X-ray photoelectron spectroscopy (XPS) analysis indicated that the improvement in the electrocatalytic activity of the PtNPs was due to partial electron transfer from Sn to Pt.

On the basis of these and other studies,[13−15] it has been established that appropriate substrates can significantly affect the properties of electrocatalytic NPs and that these effects

Received: July 28, 2018
Published: October 12, 2018

DOI: 10.1021/jacs.8b08036
J. Am. Chem. Soc. 2018, 140, 13775−13785

arise primarily from changes to either the electronic properties[14,22] or geometric structure[1,26] of the NPs. However, there is still very little understanding of how these and other effects conspire to improve electrocatalytic reaction rates or specificity.[27] Accordingly, it is, at present, not possible to *a priori* methodically tune the properties of metal NPs using support effects to achieve better electrocatalytic performance.

To address this challenge, we recently reported well-defined experimental models for studying the effects of SMSIs on electrocatalytic reactions (Scheme 1).[28,29] These models are

Scheme 1

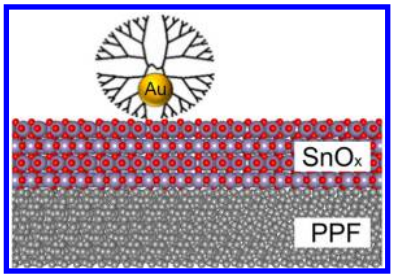

based, in part, on NP-mediated electron transfer (eT) recovery,[30−33] which permits electrochemical study of interactions between metal NPs and well-defined, ultrathin metal-oxide (MO) films. The metal NPs utilized in our studies are prepared by a dendrimer encapsulation method we[34] and others have previously reported.[35−38] These dendrimer-encapsulated NPs (DENs) are small (∼2 nm), nearly monodisperse in size, and catalytically active.[39,40] Such small NPs have two advantages. First, they are amenable to first-principles calculations, and, second, they are most likely to exhibit interesting and observable SMSI effects in catalysis.[1]

We have previously shown that when DENs are immobilized onto MO supports prepared by atomic layer deposition (ALD),[41,42] the dendrimers prevent direct interactions between the encapsulated NPs and the MO supports.[29] However, we developed a UV/O_3-based procedure that removes the dendrimer scaffolds without measurably affecting the size, shape, or composition of the encapsulated NPs.[29] Accordingly, it is possible to study electrocatalysis using exactly the same electrode in the absence and presence of direct interactions between the metal NPs and the MO supports.

We initially applied this experimental model system to what amounts to a control experiment.[29] Specifically, we examined the oxygen reduction reaction (ORR) at PtNPs in the absence and presence of interactions with an Al_2O_3 support. Alumina is not an active oxide in catalysis, and therefore we did not expect it to influence the ORR. Indeed, this is what was observed. Now we are moving into a new phase of research in which the oxide supports are specifically chosen to exhibit SMSIs and hence influence electrocatalytic reactions. Indeed, we now rely on theory to predict, in advance, combinations of metals and oxides that will yield superior performance. This interplay between theory and experiment is effective because the experimental model is nearly as well-defined as the theoretical constructs. Accordingly, there is a direct correlation between structure and function. This is important, because there are not too many examples in which first-principles theory correctly predicts the function of a complex electrocatalyst.

In the present manuscript we consider the effect of two different supports ($SnO_{1.9}$ and $SnO_{2.0}$) and one type of metal NP (Au DENs containing an average of 147 atoms, Au_{147}) on the activity of the ORR. Compared to the case wherein the AuNPs are not in contact with the oxides, calculations predicted an overpotential reduction of ∼0.30 V when the Au_{147} NPs directly interact with the SnO_x (x = 1.9 or 2.0) supports. The key finding of this article is that this prediction is borne out nearly quantitatively by companion experiments.

EXPERIMENTAL SECTION

Computational Methods. Spin-polarized DFT calculations were performed using the Vienna Ab initio Simulation Package.[43−45] The generalized gradient approximation with the Perdew−Wang (PW91) functional[46] was used to describe the exchange and correlation energy. Electron−ion interactions were treated by the projector augmented wave method.[47] In all calculations, the energy cutoff of the plane-wave basis set was 400 eV. The DFT+U method was applied to 4d orbitals of Sn ($4d^{10}5s^2$) to correct the on-site Coulomb interactions.[48] A value of U_{eff} = 3.5 eV was used to reproduce the electronic structure that has been observed experimentally.[49] Optimized structures were obtained by minimizing the forces on each ion until they fell below 0.05 eV/Å. A Bader analysis was employed to determine the local charge of atoms in the system.[50,51]

The lattice constants calculated in this work are set to a = 4.17 Å, for fcc Au, and a = 4.71 Å, c = 3.17 Å, for rutile SnO_2. AuNPs are modeled as cuboctahedral Au_{147} and Au_{55}. We considered the SnO_2(110) surface as it is the most stable surface of rutile SnO_2.[52] The SnO_2(110) surface was modeled as a 6-layer slab with the top four layers fully relaxed, and the bottom two layers fixed in bulk positions. A vacuum gap of 15 Å was used to separate the slab from its periodic images. Supercells with a periodicity of (2 × 1) were employed to calculate adsorption and electrochemical reactions on the SnO_2(110) surface. The Brillouin zone was sampled with a 4 × 4 × 1 Monkhorst−Pack k-point mesh.[53] For the hybrid Au/SnO_2(110) system, we employed a SnO_2(110) slab of three layers and a periodicity of (8 × 4) with the bottom atomic layer fixed in bulk positions. A hemispherical Au_{70} NP was placed on the surface of the SnO_2 slab. A (111) facet of the Au_{70} NP is in contact with the SnO_2(110) surface. The boundary of the NP is in registry with the bridging oxygen atoms on the SnO_2(110) surface. The uncovered area of the SnO_2(110) is terminated with adsorbed H and OH because this termination is stable in the relevant electrochemical environment, as determined by the surface phase diagram. Due to the large model employed, only the Γ point was used to sample the Brillouin zone. The atomic structures of these models are shown in Figure S-1.

Thermochemistry of the electrochemical ORR was calculated by applying the computational hydrogen electrode method.[54] This method has previously proved successful in predicting ORR activity trends on transition metal surfaces[54] and oxide surfaces.[55] Briefly, the Gibbs free energy change of each electrochemical elementary step of the ORR was calculated with DFT. The ORR reaction mechanism was assumed to follow the four-step associative mechanism represented in eqs 1−4.

$$O_2(g) + H^+ + e^- + * \leftrightarrow OOH* \quad (1)$$

$$OOH* + H^+ + e^- \leftrightarrow O* + H_2O(l) \quad (2)$$

$$O* + H^+ + e^- \leftrightarrow OH* \quad (3)$$

$$OH* + H^+ + e\_ \leftrightarrow H_2O(l) + * \quad (4)$$

The free energy change of each elementary step can be calculated as $\Delta G = \Delta E - T\Delta S + \Delta ZPE$, where ΔZPE is the zero-point energy. The total energy changes (ΔE) of these elementary steps are the energy differences between DFT-calculated energies of reactant and product states. The chemical potential of the solvated proton and electron pair ($H^+ + e^-$) at standard conditions (pH = 0, T = 298.15 K) is calculated as $1/2G_{H2} + eU_{SHE}$ assuming equilibrium at the standard hydrogen electrode. The changes in ΔZPE and $T\Delta S$ are calculated using previously determined values.[54] Using the same

DOI: 10.1021/jacs.8b08036
J. Am. Chem. Soc. 2018, 140, 13775−13785

computational hydrogen electrode method, it was also possible to calculate the surface free energies of formation of various SnO_2(110) surfaces covered with different adsorbates and determine stable surfaces as a function of applied electrode potential at pH = 0 (surface-phase diagram).[56]

Chemicals and Materials. All chemicals were used as received. These include the following: 1,1′-ferrocenedimethanol ($Fc(MeOH)_2$, 98%, Acros Organics, NY), $HClO_4$ (+70%, ultrapure grade, J. T. Baker), NaOH (Fischer Scientific), and $NaBH_4$ (99.99% trace metals basis, Sigma-Aldrich). Tetrakis(dimethylamino)tin(IV) (99%, (99.99%-Sn)) (TDMASn) for ALD was obtained in a sealed stainless-steel canister from STREM Chemicals. High-purity N_2 (99.9999%) for ALD, high-purity O_2 (99.9999%) for the UV/O_3 system, and a mixed 5% H_2/95% N_2 gas for pyrolysis of photoresists were purchased from Praxair (Austin, TX).

Quartz slides were purchased from Technical Glass Products (Painesville Twp, OH). AZ 1518 photoresist and AZ 400 K developer (prediluted 1:4) were purchased from Integrated Micro Materials (Argyle, TX). Acrylic sheets and silicone gaskets were from McMaster Carr (Atlanta, GA). NanoPorts and fluidic connections were from Idex Health and Science (Oak Harbor, WA).

Sixth-generation, amine-terminated, poly(amidoamine) dendrimers (G6-NH_2) were purchased as a 10−25% methanol solution from Dendritech, Inc. (Midland, MI). Prior to use, the methanol was removed under vacuum. National Exposure Research Laboratory (NERL) reagent-grade water from Thermo Scientific was used for the synthesis of DENs and all other aqueous solutions.

Fabrication of Pyrolyzed Photoresist Film (PPF) Electrodes. PPF electrodes were fabricated following a previously reported procedure (Supporting Information).[29]

Deposition of SnO_x (x = 1.7 or 2.0) Films onto PPF Electrodes. Oxide deposition was carried out using a Savannah S100 Cambridge NanoTech ALD system (Ultratech, San Jose, CA). TDMASn, heated to 60 °C, was used as the Sn source, and H_2O was the oxygen source. The ALD system was evacuated to <1 mmHg, and a patterned PPF substrate was heated to 150 °C for 20 min under a constant flow (20 sccm) of high-purity N_2. Each ALD cycle was carried out as follows: (1) a single 0.015 s pulse of H_2O, (2) a 30.0 s purge with N_2, (3) a 0.50 s pulse of TDMASn, and (4) a 30.0 s purge with N_2. These four steps were repeated until the desired number of cycles had been achieved. This ALD procedure results in formation of $SnO_{1.7}$ films. These films were converted into the stoichiometric oxide ($SnO_{2.0}$) by heating to 150 °C for 60 min under a constant flow of O_2 (150 sccm).

Surface Characterization. X-ray photoelectron spectroscopy (XPS) was carried out using a Kratos Axis Ultra spectrometer (Chestnut Ridge, NY) having an Al K_α source. Samples were grounded using Cu tape. Spectra were collected using a 0.10 eV step size and a band-pass energy of 20 eV. An electron flood gun was used to neutralize charge. Binding energies (BEs) were calibrated against the C 1s line of PPF (284.5 eV).[57,58] CasaXPS (version 2.3.15, Casa Software, Teignmouth, UK) was used for peak fitting and analysis. A mixed Gaussian/Lorentzian model was used for symmetric line shapes, while an asymmetric Lorentzian model was applied for asymmetric line shapes.

Ellipsometric measurements were performed using a J. A. Woollam M-2000D spectroscopic ellipsometer (Lincoln, NE). Data were collected using five different angles (between 44° and 66°) for each measurement. A three-part model was used for data analysis. The first slab was a 1.0 mm-thick layer of SiO_2 (optical constants provided by the manufacturer). The second slab was a 500 nm-thick layer of carbon (optical constants determined experimentally using a plasma-activated PPF thin film).[58] The third layer was SnO_2, and its optical constants were provided by the manufacturer. The thickness of the oxide layer was allowed to vary.

The surface roughness of the PPF and PPF/SnO_x (x = 1.7 or 2.0) thin films were obtained using a Wyko NT9100 optical profilometer having a white light source and yielding 0.1 nm vertical resolution.

Synthesis of DENs. Au DENs were synthesized using a previously published procedure.[59,60] Specifically, 200 μL of 100 μM G6-NH_2 dendrimer was added to 8.65 mL of NERL water with vigorous stirring. Next, 147 μL of a 20.0 mM $HAuCl_4$ stock solution was added dropwise. Within 2 min of adding the first drop of the $HAuCl_4$ solution, an ∼67-fold molar excess of $NaBH_4$ (in 1.0 mL of 0.30 M NaOH) was added. The reaction mixture was stirred overnight to deactivate excess $NaBH_4$. The final concentration of this 10.0 mL Au_{147} DENs solution was 2.0 μM.

Immediately before immobilizing Au DENs onto the PPF/SnO_x electrodes, the pH of the Au_{147} DENs solution was adjusted to ∼3.2 using an aqueous $HClO_4$ solution. Scanning transmission electron microscopy (STEM) indicated that Au_{147} DENs prepared in this way appeared spherical and had an average diameter of 1.8 ± 0.3 nm (Figure S-2).

Au DENs were immobilized atop SnO_x-modified PPF electrodes by immersing the latter in the Au DENs solution (pH 3.2) for 2 h, after which the electrodes were rinsed under a gentle flow of NERL water and dried under low-pressure Ar. The newly formed PPF/SnO_x/G6-NH_2(Au_{147})-modified electrodes were left to dry for at least 60 min prior to use.

UV/O_3 Method for Decomposition of G6-NH_2 Dendrimers. The G6-NH_2 dendrimers were removed from the Au_{147} DENs using a modified version of the UV/O_3 process we have described previously for the removal of the G6-OH dendrimers from Pt_{55} DENs.[61,62] This procedure is briefly described in the Supporting Information.

Electrochemical Characterization. Electrochemical measurements were performed using a CH Instruments model CHI700D bipotentiostat (Austin, TX). For all electrochemical experiments, a Hg/Hg_2SO_4 reference electrode (MSE, CH Instruments) and a Pt wire counter electrode were used. Throughout this Article, however, potentials were converted to the standard hydrogen electrode (SHE) to simplify comparison to the theoretical calculations. For static (nonflow) experiments, the electrochemical cell was fabricated from Teflon and used a Viton O-ring to define the area of the working electrode (12.4 mm^2). Prior to experiments, the Au DENs were electrochemically cleaned by scanning the potential between 0.45 and 1.55 V (vs SHE) ten times in 0.10 M $HClO_4$ solution. Electrochemical measurements were performed in aqueous solutions containing 1.0 mM $Fc(MeOH)_2$ and 0.10 M KNO_3 or 0.10 M $HClO_4$ purged with either Ar or O_2.

Some electrochemical experiments were carried out using a flow cell having a previously reported design and characteristics.[29] Measurements in the flow cell were carried out at several different flow rates. Between experiments at different flow rates 5 min was allotted for the system to stabilize.

RESULTS AND DISCUSSION

Surface-Phase Diagram of SnO_2(110). Thermodynamically stable surface structures of SnO_2(110), as a function of applied potential, were found by calculating the relative stability of different adsorbate structures on the SnO_2(110) surface. The calculated free energies for many possible surface adsorbate structures on SnO_2(110) are plotted vs potential at pH = 0 in Figure S-3. Figure S-3 shows that the most stable surface structure within the potential window of −0.25 to 1.5 V is the water-dissociated SnO_2(110) surface that consists of adsorbed OH^- species atop Sn_{5c} ($Sn_{5c}OH^-$) and hydrogenated lattice bridging oxygen ($O_{bri}H^+$). The strong electrostatic interaction between $Sn_{5c}OH^-$ and $O_{bri}H^+$ makes the water-dissociated surface stable over a wide potential window. When the applied potential is lower than −0.25 V, the most stable surface is the hydrogenated SnO_2(110) surface.

ORR Activity of SnO_2(110). The phase diagram (Figure S-3) indicates that the SnO_2(110) surface is inactive for the ORR under normal operating conditions because $Sn_{5c}OH^-$ cannot be reduced to yield water unless a potential below −0.25 V is applied. The inactivity of the SnO_2(110) surface is further illustrated by plotting the Gibbs free energy profile (FEP)

DOI: 10.1021/jacs.8b08036
J. Am. Chem. Soc. 2018, 140, 13775−13785

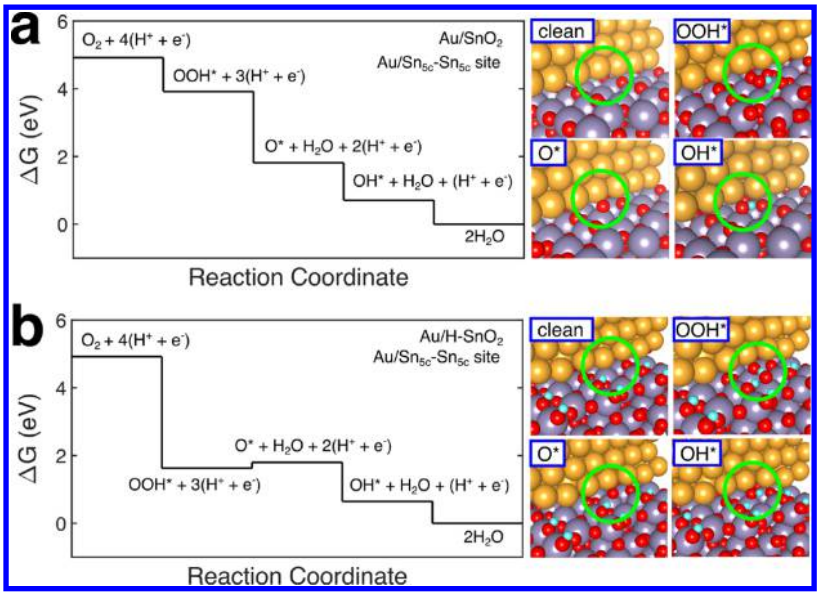

Figure 1. Free-energy diagrams for oxygen reduction on (a) the Au/Sn_{5c}-Sn_{5c} site at the interface of the Au rod/stoichiometric $SnO_2(110)$ model and (b) the Au/Sn_{5c}-Sn_{5c} site at the interface of the Au rod/hydrogenated $SnO_2(110)$ at $U = 0$, pH = 0, and $T = 298.15$ K. The atomic structures of active sites and intermediate adsorbates along the reaction coordinates are shown. "Clean" indicates the bare active site without adsorbates. "OOH*", "O*", and "OH*" are structures of adsorbates as indicated by the label. The color code is yellow for Au, red for O, purple for Sn, and cyan for H.

along the ORR coordinate. The resulting FEP is shown in Figure S-4a along with the adsorbate surface structures. The potential-determining step for the ORR on the hydrogenated $SnO_2(110)$ surface is the reduction of OH* to water, which requires a calculated overpotential of ~1.3 V.

We also investigated the ORR activity of other $SnO_2(110)$ surface structures, including the stoichiometric $SnO_2(110)$ surface and the partially reduced $SnO_2(110)$ surface having oxygen vacancies (O_v). Although these surfaces are not thermodynamically stable according to the surface-phase diagram, they could be kinetically stabilized. The FEP of the ORR on the stoichiometric $SnO_2(110)$ surface is shown in Figure S-5a. The active site examined was the top site of Sn_{5c}. The atomic structures of various reaction intermediates adsorbed on $SnO_2(110)$ are shown alongside the FEP. The top site of Sn_{5c} requires a large overpotential (~1.3 V) for the ORR due to weak binding strengths of oxygenated species, especially OOH*. Hence, the overpotential-determining step in this case is the first reduction of O_2 to form OOH*. We also examined the role of O_v for ORR catalysis. Figure S-5b shows the FEP of ORR at the O_v site on $SnO_2(110)$. The results indicate that the oxygenated species adsorbs too strongly on the O_v site, and once the O_v site is saturated with O*, the O_v site cannot be regenerated to complete the catalytic cycle.

ORR Activity of Au_{147}. Given the foregoing discussion of the ORR activity on the $SnO_2(110)$ surface, we turn our attention to the ORR on Au_{147} NPs. For Au_{147}, the FEPs of the ORR were calculated on an edge site and on (100) and (111) facet sites. The results for the edge site and the atomic structures of the adsorbed intermediates are shown in Figure S-4b. The calculations indicate that the ORR on the Au_{147} edge site requires a theoretical overpotential of about 1.0 V and that the potential-determining step is the formation of OOH*. The adsorption strengths of O* and OH* are very close to the ideal binding strength. Hence, one way to improve Au_{147} for ORR catalysis is to stabilize OOH* on Au_{147}. Finally, Figure S-6 shows the results for the (111) and (100) facets. Compared to the previously discussed edge site, the (111) and (100) facets yield higher theoretical overpotentials due to the more closely packed surfaces and correspondingly weaker adsorbate interactions.

ORR Activity of Au/SnO_2. Hybrid metal/metal-oxide systems often exhibit synergistic effects that can lead to enhancement of catalytic activity. For example, we have previously demonstrated that interfacial adsorption sites exist that can enhance the O_2 adsorption strength on Au/TiO_2 as compared to the individual Au and TiO_2 components.[8,63] In these cases, the enhancement is due to the combined effects of charge transfer and redistribution at the Au/TiO_2 interface.[8] Because the Au_{147} catalyst suffers from weak adsorption of OOH*, which leads to a high predicted ORR overpotential, combining Au with SnO_2 is a possible strategy for increasing the OOH* binding strength.

For the foregoing reason, we investigated O_2 adsorption at the interface perimeter of Au/SnO_2 using a model we used previously for studying the Au/TiO_2 interface.[8] Several adsorption sites for O_2 were examined, and the adsorption surface structures and corresponding adsorption energies are shown in Figure S-7. The results indicate that O_2 adsorbed at the Au/Sn_{5c}-Sn_{5c} site (Figure S-7a) has an appreciable adsorption energy (−0.83 eV) which is close to the calculated adsorption energy on Pt of −0.75 eV. The calculated FEP for the ORR (Figure 1a) confirms the high ORR activity at this Au/Sn_{5c}-Sn_{5c} site. The predicted theoretical overpotential is 0.5 V, which is 0.7 V lower than the Au_{147} edge sites. This is a consequence of the increased OOH* adsorption strength. We note, however, that this calculation does not take into account the SnO_2 surface structure under typical ORR operating conditions. When the SnO_2 surface is hydrogenated, as predicted by the surface-phase diagram (Figure S-3), the interfacial Au/Sn_{5c}-Sn_{5c} site no longer possesses high ORR activity, because the strong interaction between $Sn_{5c}OH^-$ and $O_{bri}H^+$ leads to poisoning of the Sn_{5c} site (Figure 1b). The other interfacial sites involving Sn_{5c}, that is the Au−Sn_{5c} dual

DOI: 10.1021/jacs.8b08036
J. Am. Chem. Soc. 2018, 140, 13775−13785

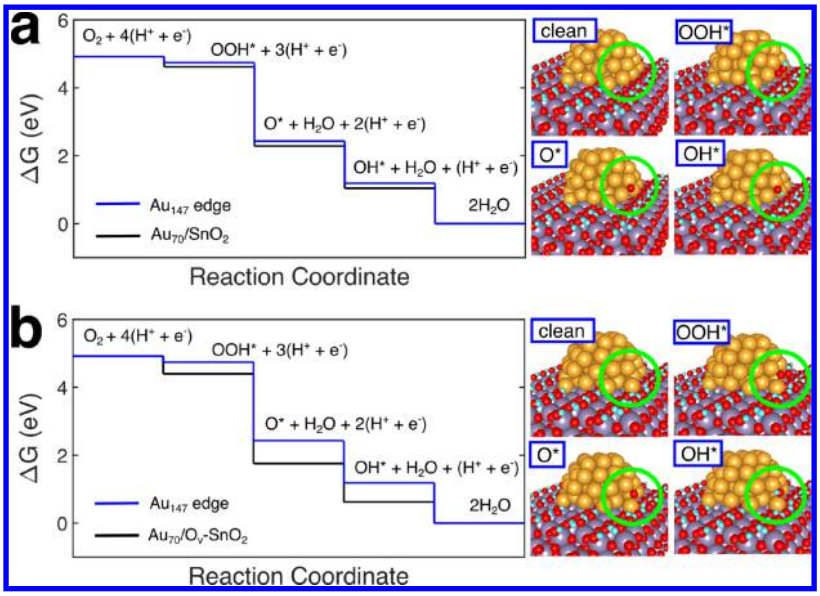

Figure 2. Free-energy diagrams for the ORR on (a) an the Au edge site of Au_{70}/water-dissociated $SnO_2(110)$ and (b) the anionic Au site of Au_{70}/water-dissociated O_v-$SnO_2(110)$ at $U = 0$, pH = 0, and $T = 298.15$ K. The atomic structures of active sites and intermediate adsorbates along the reaction coordinates are shown. "Clean" indicates the bare active site without adsorbates. "OOH*", "O*", and "OH*" are structures of adsorbates as indicated by the label. The color code is yellow for Au, red for O, purple for Sn, and cyan for H.

site and Sn_{5c}-Sn_{5c} site, suffer the same problem of strongly adsorbed OH^- atop Sn_{5c}. Therefore, our calculations exclude the interfacial sites as being active for the ORR.

The calculation represented by Figure S-7d also indicates that SnO_2 does not promote O_2 adsorption on the AuNP, even considering Au sites near the Au/SnO_2 interface. This supported Au nanorod model is designed to model the edge of a large (>3 nm) NP. Since the Au_{147} DENs are <2 nm in diameter, we also considered an isolated supported NP on the $SnO_2(110)$ surface, which better captures the different Au/$SnO_2(110)$ boundary sites. As modeling an entire supported Au_{147} NP was too computationally expensive, we used a surrogate Au_{70} hemispherical model and placed it on the water-dissociated $SnO_2(110)$ surface, which is most relevant under reaction conditions. The FEP of the ORR on the edge of Au_{70} supported on $SnO_2(110)$ is shown in Figure 2a. The predicted theoretical overpotential is close to that on the edge of unsupported Au_{147}; the limitation of both systems is the same − the lack of binding sites with sufficient adsorption energy for oxygen species, including OOH*.

SnO_2 is a prototypical transparent conductor, exhibiting the seemingly contradictory properties of high metallic conductivity, due to massive structural nonstoichiometry, with nearly complete insulator-like transparency in the visible range. First-principles calculations confirm that O vacancies and Sn interstitials have low formation energies and strong mutual attraction, which explains why SnO_2 can be found in the off-stoichiometric form, SnO_{2-x}.[64] Hence, we should expect an appreciable concentration of oxygen vacancies on the $SnO_2(110)$ surface. Additionally, the supported AuNPs should prefer to reside on surface oxygen vacancies due to stronger adsorption. To capture this effect in the Au_{70}/SnO_2 model, we introduced a surface O_v beneath an Au atom at the edge of the Au-rod model. After relaxation, the Au atom above O_v sinks into the O_v due to the strong interaction, and the Au atom is reduced to a negative charge of −0.38e, according to our Bader analysis. We further calculate the FEP of the ORR at this anionic Au site, as shown in Figure 2b. The calculated theoretical overpotential in this case is 0.7 V, which is decreased by 0.3 V as compared to that at the edge of Au_{147}. The enhancement is due to the stronger binding energy of OOH* at the anionic Au site above the surface O_v on $SnO_2(110)$ as compared to OOH* binding on the metallic Au site in Au_{147}. Thus, theory predicts that by supporting Au NPs on SnO_2 containing O_v, the ORR activity will be significantly enhanced as compared to the unsupported Au NP.

We would like to point out that the electron transferred to Au is localized on the anionic Au adsorbed on the oxygen vacancy rather than delocalized over the whole Au NP. The local nature of the electron transfer process is illustrated in Figure S-8 and the corresponding discussion.

Properties and Stability of SnO_x (x = 1.7 and 2.0). $SnO_{1.7}$ and $SnO_{2.0}$ ALD films were prepared following the detailed procedures outlined in the Experimental Section and Supporting Information. For the purposes of our experiments, the critical characteristics of these films are that they have well-defined thicknesses, that they are electrochemically passivating and stable under electrochemical conditions, and that they are uniform over macroscopic dimensions.

The thicknesses of the $SnO_{1.7}$ and $SnO_{2.0}$ films were measured using spectroscopic ellipsometry. These data reveal a linear growth rate of 0.078 ± 0.005 nm/cycle for both materials (Figure S-9).[42] This value is consistent with that reported in the literature for the deposition of SnO_2 at 150 °C onto PPF (0.078 ± 0.003 nm/cycle) and onto Si(100) (0.07 nm/cycle).[65]

We found that a thickness of 2.2 nm (28 ALD cycles) was necessary for both $SnO_{1.7}$ and $SnO_{2.0}$ to completely passivate electron transfer (eT) between the underlying PPF electrode and solution-phase $Fc(MeOH)_2$. For example, Figure 3 compares cyclic voltammograms (CVs) of PPF, PPF/$SnO_{1.7}$, PPF/$SnO_{2.0}$, PPF/$SnO_{1.7}$/G6-NH_2(Au_{147}), and PPF/$SnO_{2.0}$/G6-NH_2(Au_{147}) electrodes in the presence of 1.0 mM $Fc(MeOH)_2$. The experimental conditions for immobilization of Au_{147} DENs onto PPF/SnO_x electrodes are discussed in the Experimental Section. The CVs in Figure 3a show that while

DOI: 10.1021/jacs.8b08036
J. Am. Chem. Soc. 2018, 140, 13775−13785

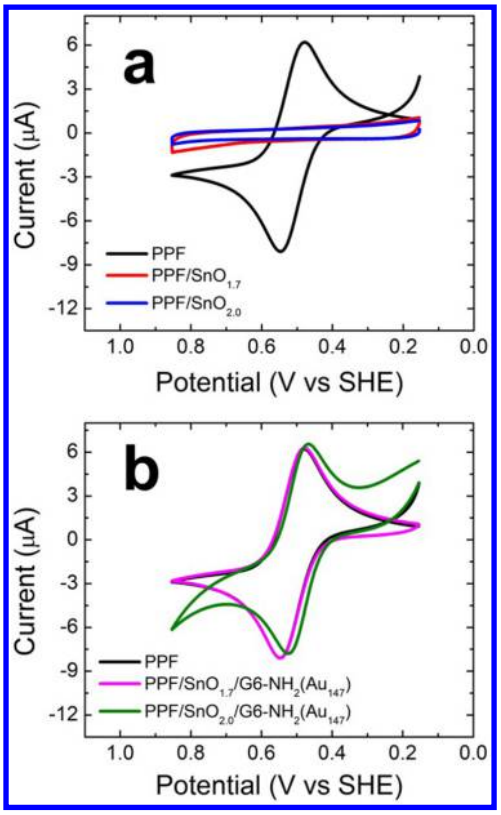

Figure 3. CVs obtained at the electrode modifications shown in the figure legends. The solutions contained aqueous 1.0 mM $Fc(MeOH)_2$ and 0.10 M KNO_3. The scan rate was 0.010 V/s. The geometric area of each electrode was 12.4 mm^2.

well-defined oxidation and reduction peaks are observed for a naked PPF electrode (black), these peaks are absent when the same electrochemical scans are carried out with either PPF/$SnO_{1.7}$ (red) or the PPF/$SnO_{2.0}$ (blue) electrodes. This clearly indicates that 2.2 nm of either $SnO_{1.7}$ or $SnO_{2.0}$ is sufficient to completely passivate eT. However, the shapes of the CVs corresponding to PPF/$SnO_{1.7}$/G6-NH_2(Au_{147}) (magenta) and PPF/$SnO_{2.0}$/G6-NH_2(Au_{147}) (green) electrodes are very similar to that of a PPF (black) electrode (Figure 3b). This finding indicates that electroactivity is completely reactivated in the presence of Au_{147} DENs.[28,30−32]

We next evaluated the stability of the PPF/SnO_x films under the electrochemical conditions used in our experiments. The Au_{147} DENs were immobilized onto the SnO_x-modified PPF electrodes at pH ∼ 3.2, and the ORR experiments were carried out in 0.10 M $HClO_4$ solution. Therefore, to determine the stability of the ALD-modified electrodes under acidic conditions, the PPF/$SnO_{1.7}$ and PPF/$SnO_{2.0}$ electrodes were immersed in 0.10 M $HClO_4$ solution for 2.0 h. Figure S-10 shows CVs of $Fc(MeOH)_2$ for the PPF/SnO_x electrodes before and after this acid treatment. Changes to the CVs are small and indicate that the ALD films are rather stable under the tested acidic conditions.

The surface roughness of SnO_x films was studied using optical profilometry, which revealed surfaces that are uniform and free of cracks. The average rms roughness of three independently prepared PPF electrodes coated with 2.2 nm-thick $SnO_{1.7}$ or $SnO_{2.0}$ determined over an area of 48 μm × 64 μm were just ∼0.63 ± 0.06 nm and ∼0.68 ± 0.04 nm, respectively (Figure S-11).

As mentioned in the Experimental Section, ALD was used to prepare the $SnO_{1.7}$ films, and the $SnO_{2.0}$ films were prepared by oxidizing the as-prepared $SnO_{1.7}$ films at 150 °C. XPS was used to determine the oxidation states of the two types of ALD films. Analysis of a SnO_x sample immediately after the ALD synthesis showed that the ratio of the atomic concentrations of Sn 3d:O 1s was 1.0:1.7 (Figure S-12a,b and Table S-1). A similar analysis was done with the ALD film following oxidation at 150 °C. In this case, the results indicate that the Sn 3d:O 1s ratio increased to 1.0:2.0 (Figure S-12c,d and Table S-1).

Decomposition of G6-NH_2 Dendrimers. In our previous studies, we showed that UV/O_3 can be used to nearly completely remove dendrimers from G6-OH(Pt_{55}) DENs immobilized onto naked PPF electrodes and PPF electrodes modified with Al_2O_3.[29,66] In the present case, we switched from G6-OH to G6-NH_2 PAMAM dendrimers because the peripheral hydroxyl groups of G6-OH can prematurely reduce the Au^{3+}/G6-OH DEN precursor complex, resulting in polydisperse AuNPs.[59] This problem is avoided if G6-NH_2 dendrimers are used.[36,59]

Accordingly, we evaluated the extent to which the G6-NH_2 dendrimers are decomposed by UV/O_3 by examining the PPF/$SnO_{1.7}$/G6-NH_2(Au_{147}) interface before and after UV/O_3 treatment. The results indicate that there is a 93% decrease of the dendrimer C 1s signal (Figure S-13a,b) and an 88% decrease in the dendrimer N 1s signal (Figure S-13c,d). The XPS results further showed that the UV/O_3 treatment does not cause significant oxidation of Au_{147} NPs. Nonetheless, to ensure that the entire AuNP is zerovalent after the UV/O_3, the electrodes were scanned 10 times between 0.45 and 1.55 V in 0.10 M $HClO_4$ to remove any surface oxide that might be present.

Effect of UV/O_3 Treatment on the Oxidation States of SnO_x Films. As mentioned in the previous section, the G6-NH_2 dendrimers are almost completely decomposed when exposed to UV/O_3, but we wondered if this treatment affects the oxidation state of SnO_x. Accordingly, we carried out a control experiment in which PPF/SnO_x substrates (no immobilized DENs) were subjected to UV/O_3 and then analyzed using XPS. Figure S-14 summarizes the results of this experiment; the key finding is that exposure of the PPF/$SnO_{1.7}$ electrode to UV/O_3 changes the Sn 3d:O 1s ratio to 1.0:1.9 (Figure S-14a,b and Table S-2). This means that after removal of the dendrimer the oxidation state of the support changes from $SnO_{1.7}$ to $SnO_{1.9}$. Accordingly, following exposure to UV/O_3, the PPF/$SnO_{1.7}$/G6-NH_2(Au_{147}) electrode is best represented as PPF/$SnO_{1.9}$/Au_{147} (Scheme 2a). This is a small change, but it is important to take it into account when comparing experimental results to theory.

In contrast to the $SnO_{1.7}$ substrate, UV/O_3 treatment did not significantly affect the oxidation state of $SnO_{2.0}$ (Scheme 2b). That is, following UV/O_3 the Sn 3d:O 1s ratio remained 1.0:2.0 (Figure S-14c,d and Table S-2). These substrates are therefore referred to henceforth as PPF/$SnO_{2.0}$/G6-NH_2(Au_{147}) and PPF/$SnO_{2.0}$/Au_{147} before and after the exposure to UV/O_3, respectively, where the only difference is the presence or absence of the G6-NH_2 dendrimers.

Evaluation of the ORR Onset Potential and Kinetics in the Absence and Presence of Contact between AuNPs and SnO_x Supports. In the previous sections we showed that dendrimers can be removed from encapsulated AuNPs, which means that it is possible to control whether or

DOI: 10.1021/jacs.8b08036
J. Am. Chem. Soc. 2018, 140, 13775−13785

Scheme 2

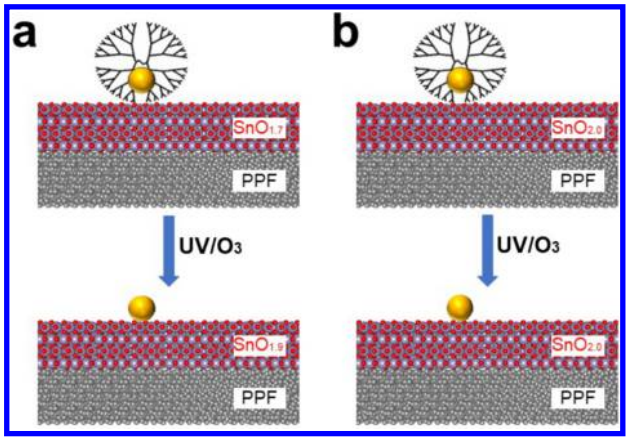

not the AuNP is in direct contact with the oxide surface (Scheme 2). Accordingly, we now focus on studying the ORR electrocatalyzed by Au_{147} NPs in the absence and presence of contact with $SnO_{1.9}$ and $SnO_{2.0}$ supports.

Prior to electrochemical measurements, the Au_{147} NPs were electrochemically cleaned as described in the Experimental Section. Figure 4 shows representative linear sweep voltammo-

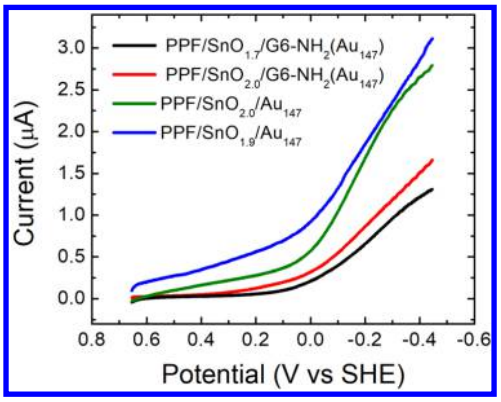

Figure 4. LSVs obtained using the indicated generator electrode (GE) modifications. The GE was scanned from 0.65 to −0.45 V (vs SHE) at 0.050 V/s in O_2-saturated 0.10 M $HClO_4$. The flow rate (V_F) was 10 μL/min. The onset potential was defined as that potential corresponding to 10% of maximum current.

grams (LSVs) for the ORR at PPF/$SnO_{1.7}$/G6-NH_2(Au_{147}) and PPF/$SnO_{2.0}$/G6-NH_2(Au_{147}) in the absence and presence of the interactions between AuNPs and the supports. These LSVs were obtained by scanning the GE electrode from 0.65 V to −0.45 at 0.050 V/s while flowing O_2-saturated 0.10 M $HClO_4$ through the flow cell (described in the Experimental Section) at 10 μL/min. As mentioned earlier, removal of the dendrimers results in direct interactions between the Au_{147} NPs and the supports. When such direct interactions are introduced between Au_{147} NPs and the $SnO_{1.9}$ support, a 0.33 V positive shift in the onset potential (defined in the figure caption) for the ORR is observed. A shift of similar magnitude (0.28 V) is observed when dendrimers are removed from the PPF/$SnO_{2.0}$/G6-NH_2(Au_{147}) electrode. The observed improvements in the onset potentials following the removal of dendrimers for both $SnO_{2.0}$ and $Sn0_{1.9}$ are in near-quantitative agreement with the calculations discussed earlier, which indicated that after the removal of the dendrimers an onset potential reduction of ∼0.30 V should be observed.

Although both $SnO_{1.9}$ and $SnO_{2.0}$ supports have a beneficial effect on the AuNP activity for the ORR, further improvements are necessary to obtain an activity similar to that of PtNPs. Specifically, following the dendrimer removal, the ORR onset potential values observed in this study are 0.48 ± 0.03 V and 0.47 ± 0.01 V (vs SHE) for PPF/$SnO_{1.9}$/Au_{147} and PPF/$SnO_{2.0}$/Au_{147}, respectively. In contrast, the ORR onset potential value that we previously observed under similar experimental conditions for PPF/Al_2O_3/Pt_{55} was ∼0.7 V (vs SHE).[29] The main point of this Article, however, is not to devise a better catalyst for the ORR but rather to experimentally evaluate the predictive power of theory.

To evaluate the kinetics of the ORR, the experiments described in the previous paragraph were repeated, but this time the flow rate of the solution in the electrochemical flow cell was varied. Figure 5 is a plot of i^{GE} vs $V_F^{1/3}$ for the

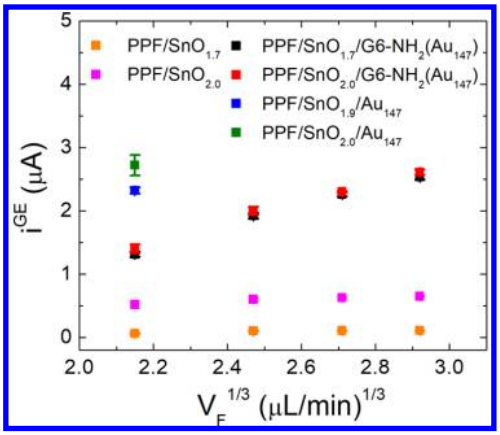

Figure 5. Plot showing the relationship between i^{GE} and $V_F^{1/3}$ for the indicated generator electrode (GE) modifications. The GE was scanned from 0.65 to −0.45 V (vs SHE) at 0.050 V/s in O_2-saturated 0.10 M $HClO_4$. The potential of the collector electrode (CE) was held at 1.35 V. The error bars represent the standard deviations for three measurements that were carried out using independently prepared electrodes.

indicated GE modifications. The value of i^{GE} is defined as the current obtained at −0.45 V. The currents for the PPF/$SnO_{1.7}$ electrode are negligible, while just slightly higher currents are observed for the PPF/$SnO_{2.0}$ electrode. In contrast, significantly higher currents are observed in the presence of the DENs (Scheme 2). It is important to point out that the currents obtained for these two types of electrode modifications (PPF/$SnO_{1.7}$/G6-NH_2(Au_{147}) and PPF/$SnO_{2.0}$/G6-NH_2(Au_{147})) overlap with each other over the entire flow rate range, indicating that the observed ORR activity is not a function of the identity of the support. This is not surprising, because the presence of the dendrimer means the DENs are not in direct contact with the oxides. We further confirmed that the identity of the oxide is not important when the dendrimers are present by carrying out the same experiments using Al_2O_3 ALD supports.[29] Indeed, the ORR currents obtained using a PPF/Al_2O_3/G6-NH_2(Au_{147}) electrode (Figure S-15) yielded results very similar to those obtained with the PPF/$SnO_{1.7}$/G6-NH_2(Au_{147}) and PPF/$SnO_{2.0}$/G6-NH_2(Au_{147}).

DOI: 10.1021/jacs.8b08036
J. Am. Chem. Soc. 2018, 140, 13775−13785

After removal of the dendrimers, further improvements in the ORR kinetics are observed for both the PPF/$SnO_{1.9}$/Au_{147} and PPF/$SnO_{2.0}$/Au_{147} electrodes. These increases are shown as the blue and green squares at $V_F^{1/3}$ = 2.15 in Figure 5. Unfortunately, these electrode modifications were not stable at higher flow rates, indicating that the dendrimer provides a stabilizing scaffold for the encapsulated DENs at higher flow rates. Nevertheless, all the results shown in Figure 5 were highly reproducible (the almost negligible error bars in the figure result from at least three trials using independently prepared electrodes), indicating that the near doubling of the current after removal of the dendrimers is real. To confirm that the increase in current results from support effects, we carried out the same experiment using an inert Al_2O_3 support. In this case, there was no change in current regardless of the presence or absence of the dendrimer (Figure S-15).

Evaluation of the ORR Pathway in the Absence and Presence of Contact between AuNPs and SnO_x Supports. In this section we describe experiments intended to better understand how the $SnO_{1.9}$ and $SnO_{2.0}$ supports affect the ORR pathway on AuNP electrocatalysts. These experiments were carried out as follows using the electrochemical flow cell in generation/collection mode. First, O_2-saturated 0.10 M $HClO_4$ was introduced into the electrochemical cell at four different flow rates (10, 15, 20, and 25 μL/min). Second, after the flow rate stabilized, the ORR was initiated at the GE by scanning it from 0.65 V to −0.45. Any H_2O_2 produced at the GE during the ORR was then detected at the CE via electrochemical oxidation. This was accomplished by holding the potential of the CE at 1.35 V.[29] The values of i^{GE} and i^{CE} obtained at −0.45 V, along with the previously determined value of collection efficiency (N = 57 ± 10%),[29] were used with eq 5 to calculate the effective number of electrons (n_{eff}) involved in the ORR.

$$n_{eff} = 4 - \frac{2i_{lim}^{CE}}{Ni_{lim}^{GE}} \quad (5)$$

Figure 6 is a plot of n_{eff} vs $V_F^{1/3}$ for the four electrode modifications indicated in the legend of the figure. Consistent with the previously discussed kinetic measurements, the values of n_{eff} nearly overlap for PPF/$SnO_{1.7}$/G6-NH_2(Au_{147}) and PPF/$SnO_{1.7}$/G6-NH_2(Au_{147}). However, when the dendrimer is removed and the AuNPs are in direct contact with the oxide, there is a dramatic reduction in the amount of peroxide generated. Specifically, n_{eff} increases from 2.1 ± 0.2 to 2.9 ± 0.1 for the PPF/$SnO_{1.7}$/G6-NH_2(Au_{147}) electrode and from 2.2 ± 0.1 to 3.1 ± 0.1 for the PPF/$SnO_{2.0}$/G6-NH_2(Au_{147}) electrode. These results indicate that direct interactions between Au_{147} NPs and both supports, $SnO_{1.9}$ and $SnO_{2.0}$, have beneficial effects on the ORR pathway.

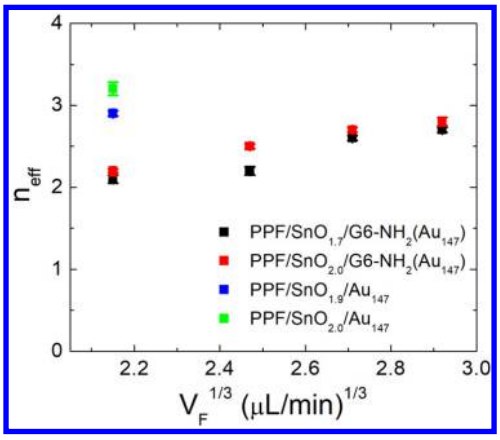

Figure 6. Plot of n_{eff} vs $V_F^{1/3}$ for the indicated electrode modifications. The potential of the collector electrode (CE) was held at 1.35 V (vs SHE). Each experiment was carried out at least three times. The error bars represent the standard deviations for three measurements that were carried out using independently prepared electrodes.

Electronic Interactions between AuNPs and SnO_x Supports. As discussed earlier, theory suggests that the reason for improvements in the ORR electrochemistry is due to electron transfer from surface oxygen vacancies within the SnO_x supports to the AuNPs, which lead to an improved binding strength of OOH* to the AuNP electrocatalysts. We next sought to confirm this theoretical result by finding experimental evidence for electronic interactions between Au_{147} NPs and the SnO_x supports. This was accomplished using XPS to determine the positions of Au 4f and Sn $3d_{5/2}$ XPS peaks before and after UV/O_3 treatment.

Before the UV/O_3 treatment, the Au 4f peaks for PPF/$SnO_{1.7}$/G6-NH_2(Au_{147}) are present at 84.31 eV (Au $4f_{7/2}$) and 88.00 eV (Au $4f_{5/2}$) (Figure 7a). These peaks are assigned to metallic Au.[57,66] Following UV/O_3 treatment and subsequent electrochemical reduction of any AuO_x that might be present, the positions of two Au 4f peaks for PPF/$SnO_{1.9}$/G6-NH_2(Au_{147}) shift by −0.28 eV so that the Au $4f_{7/2}$ peak is now observed at 84.03 eV. Similarly, the positions of the Sn $3d_{5/2}$ peaks before and after UV/O_3 (followed by electrochemical reduction of AuO_x) were found to be at 487.20 and 487.37 eV, respectively (Figure 7b). This change of +0.17 eV, taken together with the previously discussed negative shift in the Au 4f BE, indicates partial electron transfer from the $SnO_{1.9}$ support to Au_{147} NPs following removal of the dendrimer. The increased asymmetry of the Au 4f peaks following removal of the dendrimers (Figure 7a) further confirms partial charge transfer.[14]

Changes in positions of Au 4f and Sn $3d_{5/2}$ peaks were analyzed in a similar fashion for the PPF/$SnO_{2.0}$/G6-NH_2(Au_{147}) interface. Before UV/O_3 treatment, the two Au 4f peaks are present at 84.38 and 88.10 eV, corresponding to metallic Au (Figure 7c). The Sn $3d_{5/2}$ peak is at 487.14 eV (Figure 7d). Following UV/O_3 treatment, the Au 4f BEs decrease by −0.13 eV, and the Au $4f_{7/2}$ peak is now present at 84.25 eV. Following removal of the dendrimers, the Sn $3d_{5/2}$ peak shifts by +0.28 to 487.42 eV. As before, these peak shifts indicate partial electron transfer from $SnO_{2.0}$ to the Au_{147} NPs.

We previously showed that naked PPF supports and PPF/Al_2O_3 supports do not induce measurable changes in the electronic properties of Pt_{55} NPs.[29] Likewise, there was no change in the onset potential for the ORR regardless of whether the Pt_{55} NPs were in contact with PPF or PPF/Al_2O_3 interfaces. We wondered, however, if these catalytically inactive Al_2O_3 supports behave in the same way when interacting with Au_{147} NPs. Accordingly, we prepared PPF/G6-NH_2(Au_{147}) and PPF/Al_2O_3/G6-NH_2(Au_{147}) electrodes and tested them before and after UV/O_3 treatment using XPS. In both cases, negligible shifts in the positions of the peaks of interest were observed after the removal of the dendrimers. That is, in the case of PPF/G6-NH_2(Au_{147}), following the UV/O_3 treatment and subsequent electrochemical reduction, the Au 4f peaks shift by −0.04 eV toward lower BE values (Figure S-16). Similarly, in case of PPF/Al_2O_3/G6-NH_2(Au_{147}), the BEs of

DOI: 10.1021/jacs.8b08036
J. Am. Chem. Soc. 2018, 140, 13775−13785

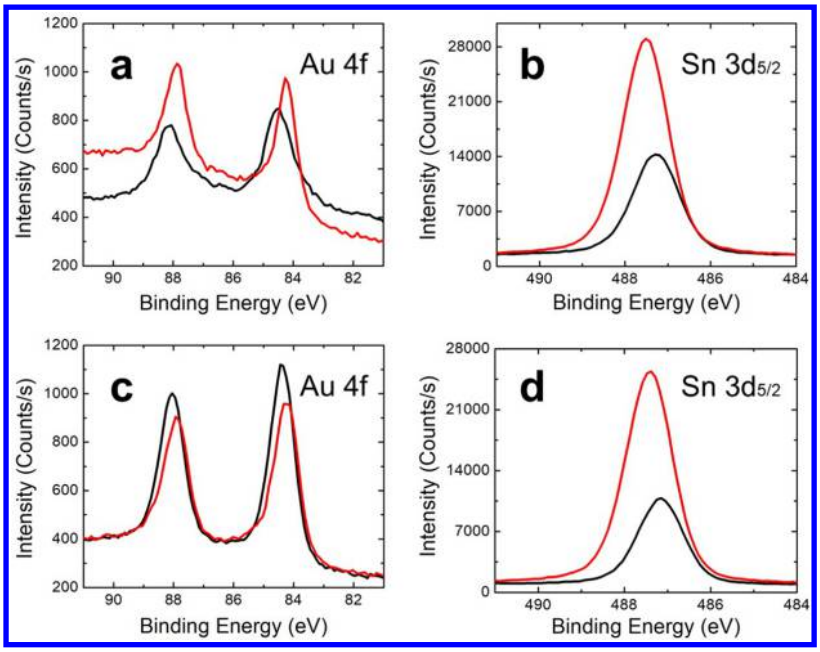

Figure 7. High-resolution XPS spectra in the Au 4f and Sn $3d_{5/2}$ regions for (a,b) PPF/$SnO_{1.7}$/G6-NH_2(Au_{147}) and (c,d) PPF/$SnO_{2.0}$/G6-NH_2(Au_{147}) electrodes before the UV/O_3 treatment (black) and after UV/O_3 treatment (followed by electrochemical reduction of Au) (red). All XPS peaks were referenced to the position of the PPF C 1s peak at 284.5 eV.

the Au 4f and Al 2s peaks shift by 0.01 and 0.05 eV, respectively (Figure S-17). These results indicate that in contrast to the $SnO_{1.9}$ and $SnO_{2.0}$ interfaces, neither the PPF nor the PPF/Al_2O_3 supports exhibit significant electronic interactions with the Au_{147} NPs. This control experiment further supports our contention of partial charge transfer from the SnO_x supports to the Au_{147} NPs.

SUMMARY AND CONCLUSIONS

Here we have shown that DFT calculations can be used to predict the nature of interactions between SnO_x thin films and AuNPs and further to understand the effect that these interactions have on the ability of AuNPs to electrocatalyze the ORR. Specifically, both theoretical predictions and subsequent experimental results have shown that enhancements in the ORR onset potential, kinetics, and pathway occur only when AuNPs directly interact with the SnO_x supports. DFT calculations and experimental results also converge to explain that the observed improvements in the ORR activity arise from electron transfer from surface oxygen vacancies within SnO_x supports to the AuNPs.

The results of this study are significant for three reasons. First, we showed that oxygen surface vacancies can have a significant effect on interactions between supports and overlaying NPs and that these interactions may have a significant impact on electrocatalytic processes. Second, we have developed a well-defined DEN/ALD experimental model that can be directly correlated to DFT calculations. Third, and most importantly, the calculations reported here were performed prior to the experiments. In other words, this study represents an unusual case of theory accurately predicting the electrocatalytic manifestation of a strong metal support interaction.

The approach described here can help broaden our understanding of the interactions between different metal NPs and metal-oxide supports and the effect of such interactions on electrocatalytic reactions. We now seek to discover if the predictive approach reported here is unique, or if it can be extended to other combinations of supports and NPs. Experiments are currently underway to determine if predictions made for a second set of materials can be confirmed experimentally. Those results will be reported in due course.

ASSOCIATED CONTENT

Supporting Information

The Supporting Information is available free of charge on the ACS Publications website at DOI: 10.1021/jacs.8b08036.

Atomic structures, Figure S-1; fabrication of pyrolyzed photoresist film (PPF) electrodes; TEM micrograph and particle-size distribution histogram, Figure S-2; UV/O_3 procedure for the removal of G6-NH_2 dendrimers from Au_{147} DENs; stable adsorbate surface structures, Figure S-3; free-energy diagram for oxygen reduction, Figure S-4; free-energy diagram for the ORR, Figures S-5 and S-6; O_2 adsorption structures and binding energies, Figure S-7; density of states of AuNP, Figure S-8; plot of ellipsometric thicknesses, Figure S-9; results of a stability test of SnO_x thin films, Figure S-10; optical profilometry of PPF electrodes, Figure S-11; high-resolution XPS spectra, Figure S-12; summary of XPS Sn 3d and O 1s atomic % concentrations/ratios, Tables S-1 and S-2; high-resolution XPS spectra, Figures S-13, S-14, S-16, and S-17; plot showing the relationship between i^{GE} and $V_F^{1/3}$, Figure S-15 (PDF)

AUTHOR INFORMATION

Corresponding Authors

*crooks@cm.utexas.edu
*henkelman@utexas.edu

ORCID

Graeme Henkelman: 0000-0002-0336-7153
Richard M. Crooks: 0000-0001-5186-4878

DOI: 10.1021/jacs.8b08036
J. Am. Chem. Soc. 2018, 140, 13775−13785

Author Contributions

†N.O. and Z.D. contributed equally.

Notes

The authors declare no competing financial interest.

■ ACKNOWLEDGMENTS

We gratefully acknowledge support from the Chemical Sciences, Geosciences, and Biosciences Division, Office of Basic Energy Sciences, Office of Science, U.S. Department of Energy (Contract: DE-SC0010576). We thank the Robert A. Welch Foundation (Grant F-0032 and F-1841) for sustained support of our research. We also thank Dr. Hugo Celio for help with data analysis.

■ REFERENCES

(1) Cuenya, B. R. Synthesis and Catalytic Properties of Metal Nanoparticles: Size, Shape, Support, Composition, and Oxidation State Effects. *Thin Solid Films* **2010**, *518* (12), 3127−3150.
(2) Liu, J. J. Advanced Electron Microscopy of Metal-Support Interactions in Supported Metal Catalysts. *ChemCatChem* **2011**, *3* (6), 934−948.
(3) Vayenas, C. G. Promotion, Electrochemical Promotion and Metal-Support Interactions: Their Common Features. *Catal. Lett.* **2013**, *143* (11), 1085−1097.
(4) Willinger, M. G.; Zhang, W.; Bondarchuk, O.; Shaikhutdinov, S.; Freund, H. J.; Schlogl, R. A Case of Strong Metal-Support Interactions: Combining Advanced Microscopy and Model Systems to Elucidate the Atomic Structure of Interfaces. *Angew. Chem., Int. Ed.* **2014**, *53* (23), 5998−6001.
(5) Tauster, S. J.; Fung, S. C.; Garten, R. L. Strong Metal-Support Interactions. Group 8 Noble Metals Supported on Titanium Dioxide. *J. Am. Chem. Soc.* **1978**, *100* (1), 170−175.
(6) Tauster, S. J. Strong Metal-Support Interactions. *Acc. Chem. Res.* **1987**, *20* (11), 389−394.
(7) Zhang, Z.; Yang, S.; Dou, M.; Liu, H.; Gu, L.; Wang, F. Systematic Study of Transition-Metal (Fe, Co, Ni, Cu) Phthalocyanines as Electrocatalysts for Oxygen Reduction and Their Evaluation by DFT. *RSC Adv.* **2016**, *6* (71), 67049−67056.
(8) Duan, Z.; Henkelman, G. CO Oxidation at the Au/TiO_2 Boundary: The Role of the Au/Ti5c Site. *ACS Catal.* **2015**, *5* (3), 1589−1595.
(9) Kim, H. Y.; Lee, H. M.; Henkelman, G. CO Oxidation Mechanism on CeO_2 -Supported Au Nanoparticles. *J. Am. Chem. Soc.* **2012**, *134* (3), 1560−1570.
(10) Ge, X.; Sumboja, A.; Wuu, D.; An, T.; Li, B.; Goh, F. W. T.; Hor, T. S. A.; Zong, Y.; Liu, Z. Oxygen Reduction in Alkaline Media: From Mechanisms to Recent Advances of Catalysts. *ACS Catal.* **2015**, *5* (8), 4643−4667.
(11) Wu, Y. Y.; Mashayekhi, N. A.; Kung, H. H. Au−metal Oxide Support Interface as Catalytic Active Sites. *Catal. Sci. Technol.* **2013**, *3* (11), 2881.
(12) Yu, L.; Liu, Y.; Yang, F.; Evans, J.; Rodriguez, J. A.; Liu, P. CO Oxidation on Gold-Supported Iron Oxides: New Insights into Strong Oxide-Metal Interactions. *J. Phys. Chem. C* **2015**, *119* (29), 16614−16622.
(13) Hsieh, B. J.; Tsai, M. C.; Pan, C. J.; Su, W. N.; Rick, J.; Chou, H. L.; Lee, J. F.; Hwang, B. J. Tuning Metal Support Interactions Enhances the Activity and Durability of TiO_2-Supported Pt Nanocatalysts. *Electrochim. Acta* **2017**, *224*, 452−459.
(14) Lewera, A.; Timperman, L.; Roguska, A.; Alonso-Vante, N. Metal−Support Interactions between Nanosized Pt and Metal Oxides (WO_3 and TiO_2) Studied Using X-Ray Photoelectron Spectroscopy. *J. Phys. Chem. C* **2011**, *115* (41), 20153−20159.
(15) Axnanda, S.; Zhou, W.-P.; White, M. G. CO Oxidation on Nanostructured SnOx/Pt(111) Surfaces: Unique Properties of Reduced SnO_x. *Phys. Chem. Chem. Phys.* **2012**, *14*, 10207−10214.
(16) Sasaki, K.; Zhang, L.; Adzic, R. R. Niobium Oxide-Supported Platinum Ultra-Low Amount Electrocatalysts for Oxygen Reduction. *Phys. Chem. Chem. Phys.* **2008**, *10* (1), 159−167.
(17) Moghaddam, R. B.; Pickup, P. G. Support Effects on the Oxidation of Ethanol at Pt Nanoparticles. *Electrochim. Acta* **2012**, *65*, 210−215.
(18) Dole, H. A. E.; Safady, L. F.; Ntais, S.; Couillard, M.; Baranova, E. A. Electrochemically Enhanced Metal-Support Interaction of Highly Dispersed Ru Nanoparticles with a CeO_2 Support. *J. Catal.* **2014**, *318*, 85−94.
(19) Wang, Y.; Widmann, D.; Behm, R. J. Influence of TiO_2 Bulk Defects on CO Adsorption and CO Oxidation on Au/TiO_2: Electronic Metal-Support Interactions (EMSIs) in Supported Au Catalysts. *ACS Catal.* **2017**, *7* (4), 2339−2345.
(20) Zhou, W. P.; Axnanda, S.; White, M. G.; Adzic, R. R.; Hrbek, J. Enhancement in Ethanol Electrooxidation by SnO_x Nanoislands Grown on Pt (111): Effect of Metal Oxide−Metal Interface Sites. *J. Phys. Chem. C* **2011**, *115* (33), 16467−16473.
(21) Kowal, A.; Li, M.; Shao, M.; Sasaki, K.; Vukmirovic, M. B.; Zhang, J.; Marinkovic, N. S.; Liu, P.; Frenkel, A. I.; Adzic, R. R. Ternary Pt/Rh/SnO2 Electrocatalysts for Oxidizing Ethanol to CO_2. *Nat. Mater.* **2009**, *8* (4), 325−330.
(22) Jimenez-Morales, I.; Cavaliere, S.; Jones, D.; Rozière, J. Strong Metal-Support Interaction Improves Activity and Stability of Pt Electrocatalysts on Doped Metal Oxides. *Phys. Chem. Chem. Phys.* **2018**, *20*, 8765.
(23) Timperman, L.; Lewera, A.; Vogel, W.; Alonso-Vante, N. Nanostructured Platinum Becomes Alloyed at Oxide-Composite Substrate. *Electrochem. Commun.* **2010**, *12* (12), 1772−1775.
(24) Park, S.; Lim, H.; Kim, Y. Enhanced Oxygen Reduction Reaction Activity Due to Electronic Effects between Ag and Mn_3O_4 in Alkaline Media. *ACS Catal.* **2015**, *5* (7), 3995−4002.
(25) Zhou, W.-P.; An, W.; Su, D.; Palomino, R.; Liu, P.; White, M. G.; Adzic, R. R. Electrooxidation of Methanol at SnOx-Pt Interface: A Tunable Activity of Tin Oxide Nanoparticles. *J. Phys. Chem. Lett.* **2012**, *3*, 3286−3290.
(26) Liu, J. J. Advanced Electron Microscopy of Metal − Support Interactions in Supported Metal Catalysts. *ChemCatChem* **2011**, *3*, 934−948.
(27) Mistry, H.; Varela, A. S.; Kühl, S.; Strasser, P.; Cuenya, B. R. Nanostructured Electrocatalysts with Tunable Activity and Selectivity. *Nat. Rev. Mater.* **2016**, *1*, 1−14.
(28) Ostojic, N.; Thorpe, J. H.; Crooks, R. M. Electron Transfer Facilitated by Dendrimer-Encapsulated Pt Nanoparticles Across Ultrathin, Insulating Oxide Films. *J. Am. Chem. Soc.* **2016**, *138*, 6829−6837.
(29) Anderson, M. J.; Ostojic, N.; Crooks, R. M. Microelectrochemical Flow Cell for Studying Electrocatalytic Reactions on Oxide-Coated Electrodes. *Anal. Chem.* **2017**, *89* (20), 11027−11035.
(30) Chazalviel, J.-N.; Allongue, P. On the Origin of the Efficient Nanoparticle Mediated Electron Transfer across a Self-Assembled Monolayer. *J. Am. Chem. Soc.* **2011**, *133* (4), 762−764.
(31) Kissling, G. P.; Miles, D. O.; Fermín, D. J. Electrochemical Charge Transfer Mediated by Metal Nanoparticles and Quantum Dots. *Phys. Chem. Chem. Phys.* **2011**, *13* (48), 21175−21185.
(32) Gooding, J. J.; Alam, M. T.; Barfidokht, A.; Carter, L. Nanoparticle Mediated Electron Transfer across Organic Layers: From Current Understanding to Applications. *J. Braz. Chem. Soc.* **2014**, *25* (3), 418−426.
(33) Hill, C. M.; Kim, J.; Bard, A. J. Electrochemistry at a Metal Nanoparticle on a Tunneling Film: A Steady-State Model of Current Densities at a Tunneling Ultramicroelectrode. *J. Am. Chem. Soc.* **2015**, *137* (35), 11321−11326.
(34) Zhao, M.; Sun, L.; Crooks, R. M. Preparation of Cu Nanoclusters within Dendrimer Templates. *J. Am. Chem. Soc.* **1998**, *120* (19), 4877−4878.
(35) Lhenry, S.; Jalkh, J.; Leroux, Y. R.; Ruiz, J.; Ciganda, R.; Astruc, D.; Hapiot, P. Tunneling Dendrimers Enhancing Charge Transport

DOI: 10.1021/jacs.8b08036
J. Am. Chem. Soc. 2018, 140, 13775−13785

through Insulating Layer Using Redox Molecular Objects. *J. Am. Chem. Soc.* **2014**, *136* (52), 17950−17953.
(36) Myers, V. S.; Weir, M. G.; Carino, E. V.; Yancey, D. F.; Pande, S.; Crooks, R. M. Dendrimer-Encapsulated Nanoparticles: New Synthetic and Characterization Methods and Catalytic Applications. *Chem. Sci.* **2011**, *2* (9), 1632.
(37) Bronstein, L. M.; Shifrina, Z. B. Dendrimers as Encapsulating, Stabilizing, or Directing Agents for Inorganic Nanoparticles. *Chem. Rev.* **2011**, *111*, 5301−5344.
(38) Zhao, P.; Li, N.; Astruc, D. State of the Art in Gold Nanoparticle Synthesis. *Coord. Chem. Rev.* **2013**, *257* (3−4), 638−665.
(39) Yeung, L. K.; Lee, C. T., Jr.; Johnston, K. P.; Crooks, R. M. Catalysis in Supercritical CO2 Using Dendrimer-Encapsulated Palladium Nanoparticles. *Chem. Commun.* **2001**, No. 21, 2290−2291.
(40) Oh, S. K.; Niu, Y.; Crooks, R. M. Size-Selective Catalytic Activity of Pd Nanoparticles Encapsulated within End-Group Functionalized Dendrimers. *Langmuir* **2005**, *21* (22), 10209−10213.
(41) George, S. M. Atomic Layer Deposition: An Overview. *Chem. Rev.* **2010**, *110*, 111−131.
(42) Nazarov, D.; Bobrysheva, N. P.; Osmolovskaya, O. M.; Osmolovsky, M. G.; Smirnov, V. M. Atomic Layer Deposition of Tin Dioxide Nanofilms: A Review. *Rev. Adv. Mater. Sci.* **2015**, *40*, 262−275.
(43) Kresse, G.; Hafner, J. *Ab Initio* Molecular Dynamics for Liquid Metals. *Phys. Rev. B: Condens. Matter Mater. Phys.* **1993**, *47* (1), 558−561.
(44) Kresse, G.; Furthmüller, J. Efficiency of Ab-Initio Total Energy Calculations for Metals and Semiconductors Using a Plane-Wave Basis Set. *Comput. Mater. Sci.* **1996**, *6* (1), 15−50.
(45) Kresse, G.; Furthmüller, J. Efficient Iterative Schemes for *Ab Initio* Total-Energy Calculations Using a Plane-Wave Basis Set. *Phys. Rev. B: Condens. Matter Mater. Phys.* **1996**, *54* (16), 11169−11186.
(46) Perdew, J. P.; Wang, Y. Accurate and Simple Analytic Representation of the Electron-Gas Correlation Energy. *Phys. Rev. B: Condens. Matter Mater. Phys.* **1992**, *45* (23), 13244−13249.
(47) Blöchl, P. E. Projector Augmented-Wave Method. *Phys. Rev. B: Condens. Matter Mater. Phys.* **1994**, *50* (24), 17953−17979.
(48) Dudarev, S. L.; Botton, G. A.; Savrasov, S. Y.; Humphreys, C. J.; Sutton, A. P. Electron-Energy-Loss Spectra and the Structural Stability of Nickel Oxide: An LSDA+U Study. *Phys. Rev. B: Condens. Matter Mater. Phys.* **1998**, *57* (3), 1505−1509.
(49) Singh, A. K.; Janotti, A.; Scheffler, M.; Van de Walle, C. G. Sources of Electrical Conductivity in SnO_2. *Phys. Rev. Lett.* **2008**, *101* (5), 055502.
(50) Henkelman, G.; Arnaldsson, A.; Jónsson, H. A Fast and Robust Algorithm for Bader Decomposition of Charge Density. *Comput. Mater. Sci.* **2006**, *36* (3), 354−360.
(51) Tang, W.; Sanville, E.; Henkelman, G. A Grid-Based Bader Analysis Algorithm without Lattice Bias. *J. Phys.: Condens. Matter* **2009**, *21* (8), 084204.
(52) Mulheran, P. A.; Harding, J. H. The Stability of SnO_2 Surfaces. *Modell. Simul. Mater. Sci. Eng.* **1992**, *1* (1), 39−43.
(53) Monkhorst, H. J.; Pack, J. D. Special Points for Brillouin-Zone Integrations. *Phys. Rev. B* **1976**, *13* (12), 5188−5192.
(54) Nørskov, J. K.; Rossmeisl, J.; Logadottir, A.; Lindqvist, L.; Kitchin, J. R.; Bligaard, T.; Jónsson, H. Origin of the Overpotential for Oxygen Reduction at a Fuel-Cell Cathode. *J. Phys. Chem. B* **2004**, *108* (46), 17886−17892.
(55) Su, H.-Y.; Gorlin, Y.; Man, I. C.; Calle-Vallejo, F.; Nørskov, J. K.; Jaramillo, T. F.; Rossmeisl, J. Identifying Active Surface Phases for Metal Oxide Electrocatalysts: A Study of Manganese Oxide Bi-Functional Catalysts for Oxygen Reduction and Water Oxidation Catalysis. *Phys. Chem. Chem. Phys.* **2012**, *14* (40), 14010.
(56) Hansen, H. A.; Rossmeisl, J.; Nørskov, J. K. Surface Pourbaix Diagrams and Oxygen Reduction Activity of Pt, Ag and Ni(111) Surfaces Studied by DFT. *Phys. Chem. Chem. Phys.* **2008**, *10* (25), 3722.
(57) *NIST X-Ray Photoelectron Spectroscopy Database*, Version 4.1; National Institute of Standards and Technology: Gaithersburg, MD. http://srdata.nist.gov/xps/ (accessed Sept 28, 2018).
(58) Loussaert, J. A.; Fosdick, S. E.; Crooks, R. M. Electrochemical Properties of Metal-Oxide-Coated Carbon Electrodes Prepared by Atomic Layer Deposition. *Langmuir* **2014**, *30* (45), 13707−13715.
(59) Kim, Y.-G.; Oh, S.-K.; Crooks, R. M. Preparation and Characterization of 1 - 2 nm Dendrimer-Encapsulated Gold Nanoparticles Having Very Narrow Size Distributions. *Chem. Mater.* **2004**, *16* (18), 167−172.
(60) Trindell, J. A.; Clausmeyer, J.; Crooks, R. M. Size Stability and H_2/CO Selectivity for Au Nanoparticles during Electrocatalytic CO2Reduction. *J. Am. Chem. Soc.* **2017**, *139* (45), 16161−16167.
(61) Yancey, D. F.; Zhang, L.; Crooks, R. M.; Henkelman, G. Au@Pt Dendrimer Encapsulated Nanoparticles as Model Electrocatalysts for Comparison of Experiment and Theory. *Chem. Sci.* **2012**, *3* (4), 1033.
(62) Anderson, R. M.; Yancey, D. F.; Zhang, L.; Chill, S. T.; Henkelman, G.; Crooks, R. M. A Theoretical and Experimental Approach for Correlating Nanoparticle Structure and Electrocatalytic Activity. *Acc. Chem. Res.* **2015**, *48* (5), 1351−1357.
(63) Duan, Z.; Henkelman, G. Calculations of CO Oxidation over a Au/TiO_2 Catalyst: A Study of Active Sites, Catalyst Deactivation, and Moisture Effects. *ACS Catal.* **2018**, *8* (2), 1376−1383.
(64) Kılıç, Ç.; Zunger, A. Origins of Coexistence of Conductivity and Transparency in SnO2. *Phys. Rev. Lett.* **2002**, *88* (9), 095501.
(65) Cambridge NanoTech, Simply ALD. www.cambridgenanotech.com (accessed May 4, 2018).
(66) Ostojic, N.; Crooks, R. M. Electrocatalytic Reduction of Oxygen on Platinum Nanoparticles in the Presence and Absence of Interactions with the Electrode Surface. *Langmuir* **2016**, *32*, 9727−9735.

DOI: 10.1021/jacs.8b08036
J. Am. Chem. Soc. 2018, 140, 13775−13785